

# Kinematical analysis of the ionized gas in the nuclear region of NGC 4214

**J. Maíz-Apellániz<sup>1,2</sup>, C. Muñoz-Tuñón<sup>3</sup>, G. Tenorio-Tagle<sup>4</sup>, and J. M. Mas-Hesse<sup>1</sup>**

<sup>1</sup> Laboratorio de Astrofísica Espacial y Física Fundamental - INTA, POB 50727, E-28080 Madrid, Spain.

<sup>2</sup> Departamento de Matemáticas y Física Aplicada, Universidad Alfonso X el Sabio, E-28691 Villanueva de la Cañada, Madrid, Spain.

<sup>3</sup> Instituto de Astrofísica de Canarias, E-38200 La Laguna, Tenerife, Spain.

<sup>4</sup> Instituto Nacional de Astrofísica, Óptica y Electrónica, Apartado Postal 51, 72000 Puebla, México.

Accepted 2 December 1998

**Abstract.** We present in this paper a detailed study of the kinematical properties of the ionized gas around the young massive star clusters in the nucleus of NGC 4214. The analysis is based on bidimensional spectroscopical data, allowing to derive the spatial variation of different properties (intensity, velocity and width / line splitting) of the emission lines H $\alpha$  and [O III]  $\lambda 5007$  along the nuclear region. We have found that the Giant H II region around the two most massive clusters in NGC 4214 (A and B) is resolved into two clearly separated regions. We have not detected superbubbles with the properties we would expect according to the evolutionary state of the stellar clusters, but just a partial ring feature around the most massive one and two expanding shells around cluster B. The first expanding shell seems to have experienced blowout, whereas the second one is still complete. A possible explanation to this phenomenon is that the most massive stars in a starburst spend a large fraction of their lives buried inside their original molecular clouds. Champagne flows might have formed at the borders of the regions, especially on the SE complex, explaining the existence of the diffuse ionized gas around the galaxy. As a consequence of these results we postulate that NGC 4214 is indeed a dwarf spiral galaxy, with a thin ( $\sim 200$  pc) disk that inhibits the formation of large scale structures in the ISM. The mechanical input deposited by the star formation complexes, in a variety of physical processes that include the free expanding bubbles liberated after blowout and photoevaporation of the parent clouds, have succeeded in generating the structures now detected far from the disk, giving place to the large-scale structure which now enriches the optical appearance of the galaxy.

## 1. Introduction

Magellanic irregular galaxies are excellent laboratories for the study of massive star formation and its impact on the surrounding interstellar medium due to the large number of Giant H II Regions (GHIRs) that they host. For example, more than 40 GEHRs have been studied and catalogued along the central bar

of NGC 4449 (Muñoz-Tuñón et al. 1998). Magellanic irregulars are also particularly rich in gas (Hunter & Gallagher 1990) and usually present an extended emission of Diffuse Ionized Gas (DIG), most probably ionized by photons escaping from the GHIRs (Muñoz-Tuñón et al. 1998). Also, superimposed on the DIG, kiloparsec-scale filaments, bubbles, and shells can be found (termed as “froth” by Hunter & Gallagher (1990)) and are most probably remnants of past star formation episodes. Further evidence supporting the idea of one or more past star formation episodes rests on the presence of Faint Extended Broad Emission Lines (FEBELs) detected on some of these irregular galaxies. The presence of FEBELs is probably linked to the low metallicity of these objects (Tenorio-Tagle et al. 1997).

In this paper we deal with NGC 4214. This galaxy has been classified as SBmIII by Sandage & Bedke (1985), but is frequently considered a typical Magellanic irregular. It shows important star formation activity along a bar-like structure across its nucleus. In a previous article (Maíz-Apellániz et al. 1998, hereafter Paper I) we used bidimensional spectroscopy to study the excitation and density of the gas as well as its distribution relative to the stars and dust. In Paper I we described the existence of two star-forming regions: the larger ( $\sim 13,000$  OB stars), slightly older (3.0-3.5 Myr) NW complex and the smaller ( $\sim 4,000$  OB stars), slightly younger SE complex. The NW complex is often named in the literature NGC 4214-I, and the SE complex, NGC 4214-II. The age of each complex was determined comparing four different parameters ( $W(H\beta)$ ,  $W(WR)$ ,  $I(WRbump)/I(H\beta)$ , and  $T_{eff}$ ) with the predictions of synthesis models (Cerviño & Mas-Hesse 1994). The consistency of our age determination using different methods indicates that the number of ionizing photons destroyed by dust or escaping from the star forming region might be large but less than half of the total ( $\approx 30\%$ ). The slightly younger age and smaller size of the SE complex is consistent with its morphology: three continuum knots with coincident H $\alpha$  emission maxima surrounded by dusty clouds. On the other hand, the NW complex displays a more complicated structure. It shows two main continuum knots surrounded by several H $\alpha$  knots and an extended halo with dust detected only at its borders. Also vis-

ible at the NW complex are two  $\text{H}\alpha$  minima located close to each of the two continuum knots.

In this paper we continue our study of NGC 4214 analyzing the kinematical properties of the ionized gas using bidimensional spectroscopy. The spatial variations in intensity, velocity and velocity dispersion ( $\sigma$ ) and the presence of anomalous kinematical components in the gas emission, in combination with the results of Paper I, allow us to produce an overall picture of the starbursts in NGC 4214. In Section 2 we present our observations and explain the reduction procedure. The results are presented in Section 3 and discussed in Section 4.

## 2. Observations and Data Analysis

Optical long-slit spectra of NGC 4214 were obtained on April 19-20/1992 with the ISIS spectrograph of the William Herschel Telescope, as described in Paper I. The spectra were obtained at twelve parallel positions, all of them at a P.A. of  $150^\circ$ , which almost coincides with the galaxy minor axis as well as with the orientation of the present day star-forming regions along the bar-like structure. The effective width for each slit was  $1''$  and the spacing between the centers of consecutive positions was set equal to  $2''$  (see Fig. 1 in Paper I).

Two spectra were taken simultaneously at each position, one in the range between 6390 and 6840 Å (red arm) and the other one in the range between 4665 and 5065 Å (blue arm), both of them with a dispersion of approximately 0.4 Å/pixel, with the intention of studying  $\text{H}\alpha$  and  $[\text{O III}] \lambda 5007$  simultaneously. The spatial resolution along the slit was  $0''.34/\text{pixel}$  and  $0''.36/\text{pixel}$  for the red and blue spectra, respectively. The seeing varied between  $0''.7$  and  $1''.0$ . This observational setup produces a three dimensional (2D spatial + 1D frequency) data set that can be arranged as a series of high dispersion spectra associated to a regular array of points in a map. The  $x$  axis runs along the slit from NW to SE and the  $y$  axis increases with slit number, from NE to SW. The origin is fixed in such a way that the first point in each slit is centered at  $x = 1/3''$  and the first slit is centered at  $y = 2''$  (thus, the last slit is centered at  $y = 24''$ ).

The data reduction was done using standard IRAF packages and our own procedures at the LAEFF SUN-Unix environment. Both atmospheric emission lines and reference neon and copper lamps were used to calibrate our spectra in wavelength. The combined data lead to an estimation of the absolute errors in the wavelength calibration of  $0.04$  Å and  $0.08$  Å for the red and blue spectra, respectively.

The instrumental width of the lines,  $\sigma_{\text{inst}}$ , was  $11.6 \pm 0.8$  km s $^{-1}$  and  $20.9 \pm 0.8$  km s $^{-1}$  for the red and blue spectra, respectively. The lower instrumental width combined with the longer wavelength for a similar dispersion leads to a better resolution in velocity for the red spectra when compared to the blue spectra. As a consequence of this, many points in the red spectra which in  $\text{H}\alpha$  showed non-single-Gaussian profiles (i.e. which showed multiple velocity components) appeared blended into a single Gaussian, or almost Gaussian, profile in  $[\text{O III}] \lambda 5007$ . Visible multiple components were quite scarce in  $[\text{O III}] \lambda 5007$  and this dearth allowed us to extract the

$[\text{O III}] \lambda 5007$  kinematical information by fitting a single Gaussian profile for each point. This was done using the automatic *fitlines* package developed by José Acosta at the Instituto de Astrofísica de Canarias. On the other hand, the existence of multiple components in  $\text{H}\alpha$  required a manual fitting for each point with one to three Gaussians using the *splot* package. Both for  $[\text{O III}] \lambda 5007$  and  $\text{H}\alpha$  a 3 pixel smoothing in the spatial direction was performed before the (single or multiple) Gaussian fitting in order to obtain a better signal-to-noise ratio.

This combined strategy produced values for the flux,  $\sigma_{\text{obs}}$  (observed width) and center for each of the measured Gaussian components (one for  $[\text{O III}] \lambda 5007$ , one to three for  $\text{H}\alpha$ ) at each point. From those values, bidimensional tables of intensity (flux per unit solid angle),  $\sigma$  (width due to random motions, see Muñoz-Tuñón 1994) and central velocity  $v$  were obtained. The relation between the observed ( $\sigma_{\text{obs}}$ ) and the adopted line width  $\sigma$  is given by:

$$\sigma^2 = \sigma_{\text{obs}}^2 - \sigma_{\text{inst}}^2 - \sigma_{\text{th}}^2, \quad (1)$$

where  $\sigma_{\text{th}}$  is the thermal width. Following Kobulnicky & Skillman (1996), the temperature was taken to be  $10,500 \pm 500$  K in all observed regions.

Estimated errors were computed for  $\sigma$  and  $v$ . The error sources considered for  $\sigma$  were: Direct measurement error (provided by the *fitlines* package), uncertainty in the instrumental width and uncertainty in the temperature. The error sources considered for  $v$  were: Direct measurement error (provided by the *fitlines* package) and calibration error. For most cases, the direct measurement error was not important. However, there are some positions where the strong blending of the lines increased it significantly.

## 3. The Gas Dynamics of NGC 4214

Fig. 1 shows the  $\text{H}\alpha$  map of NGC 4214, which was already described in Paper I. Here we use it as a reference for the presentation and discussion of our spectroscopic results and to indicate the main features of NGC 4214. Big asterisks indicate the location of the optical continuum maxima or the location of the ionizing clusters (A,B,C following the nomenclature from Paper I). The two large H II regions lying along the optical bar – which coincides with the galaxy’s minor axis as defined in the H I map (McIntyre, 1998) – are clearly seen. The largest one, NGC 4214-I (or NW complex), located around the optical-UV nucleus (Fanelli et al. 1997) is at horizontal coordinates  $x = 60''$  to  $x = 100''$  while the second one, NGC 4214-II (or SE complex), extends from  $x = 100''$  to  $x = 120''$  (see Fig. 1). Note that the right hand side of the map was drawn with a lower intensity threshold to unveil the much lower intensity emission features found at large distances from the galaxy nucleus. Threshold values are indicated in the figure caption.

On the map we have marked several zones which have been analysed in detail. The first one, zone 1, covers an area of  $13'' \times 12''$  (equivalent to  $260 \text{ pc} \times 240 \text{ pc}$ ) and includes the optical-UV nucleus of the galaxy and the brightest  $\text{H}\alpha$  emitting area of

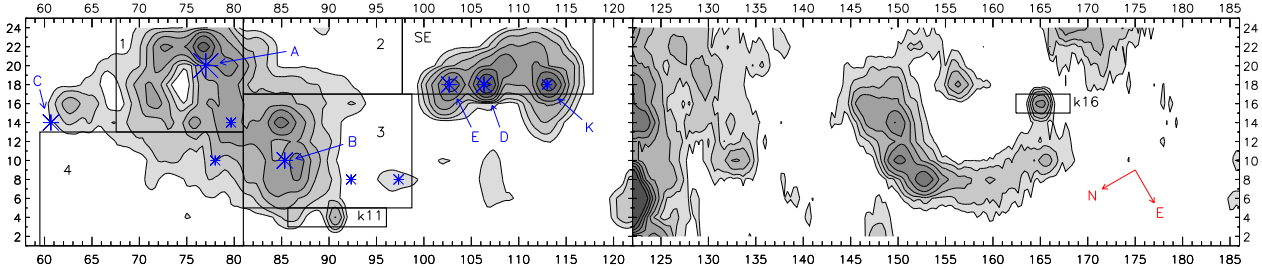


**Fig. 1.** H $\alpha$  synthetic map of NGC 4214 obtained from long-slit spectra. The left side corresponds to the sites of most intense star formation and has a minimum contour value of  $300 \cdot 10^{-17}$  erg s $^{-1}$  cm $^{-2}$  arcsec $^{-2}$  and a maximum of 7500 in these units, with the other six levels logarithmically spaced. The right side, where H $\alpha$  emission is much weaker, has minimum and maximum values of 20 and 300 (note that the minimum contour on the left is the maximum contour on the right), with the other six levels also logarithmically spaced. The axes are labelled in arcseconds with respect to the first pixel of the first slit ( $1'' = 20$  pc), with  $x$  in the horizontal direction and  $y$  in the vertical direction (see text). This coordinate system will be used throughout this work. The regions of interest have been marked as 1, 2, 3, 4, k11 (altogether known as the NW complex or NGC 4214-I), SE (the SE complex or NGC 4214-II) and k16. The asterisks indicate the location of the continuum knots, the size being a measurement of their intensity. The continuum knots referenced in the text are labelled as A, B, C, D, E and K (see Paper I).

NGC 4214-I which includes the bright H $\alpha$  knots 3, 7, 8, 9 and 10 (according to the nomenclature used in Paper I).

Zone 2 covers an area of  $16'' \times 8''$  (equivalent to  $320$  pc  $\times$   $160$  pc) towards the southeastern border of zone 1 and spans the lower intensity area at the optical SW edge of the bar, where Hunter & Gallagher (1990) detected the filamentary low emission structures or “froth” features, emanating from the central regions of the galaxy.

Zone 3 covers a similar size area and contains most of NGC 4214-I not included in zone 1; the bright H $\alpha$  knots 5 and 6 – see Paper I – as well as continuum knot B. Zone 4 traces the background H $\alpha$  emission at the northern border of NGC 4214-I. Knot C was not included in any zone because it is an apparently older cluster which has almost no gas in its surroundings. The only remaining part of the original ionized cloud is located some 70 pc towards the south of the cluster. This cloud does not show any important kinematical difference with its surroundings and, therefore, will not be studied in this section.

We have also analyzed the spectra of the three main H $\alpha$  knots of NGC 4214-II (zone SE) and that of two small but intense and peculiar emitting knots. One of these is on the border of NGC 4214-I (k11) and the second one (k16) is a low intensity emitting region  $50''$  (1 kpc) away from NGC 4214-II.

The H $\alpha$  emission line for each of the spectra included in the marked areas has been analyzed by fitting either one, two or three Gaussian profiles and from these we derived intensity, velocity and  $\sigma$  values (see the previous section). The parameters have been plotted as a function of position along each of the slits that traverses the marked zones. All velocity dispersion ( $\sigma$ ) values have been corrected for instrumental and thermal broadening. The velocity reference has been taken from the H I map (McIntyre, 1998). From this map, the heliocentric velocity at the nucleus is  $300$  km s $^{-1}$ . This value has been subtracted to all measured velocity centroids presented in this paper.

### 3.1. NGC 4214-I (the NW complex)

The largest star-forming complex, NGC 4214-I, is covered by zones 1, 2, 3 and 4 (see Fig. 1) all of them presenting different gas dynamical properties.

#### 3.1.1. Zone 1

Fig. 2 shows the results in H $\alpha$  corresponding to the six slits (7 to 12) that traverse zone 1. At several spatial positions, up to three line emission components have been identified, and their intensities and velocities are also represented in the figures. Diamond symbols have been used to indicate marginal detections. As an example, Fig. 3 shows four spectra extracted from slit 9. The spectrum in Fig. 3a shows a clear and well resolved two component splitting. Fig. 3b is a clear case with three resolved components and Figs. 3c and d are examples of marginal detections: a blue secondary component in 3c and a red one in case 3d. No attempt has been made to assign a  $\sigma$  value to the secondary components. However, large  $\sigma$  values of the main emission line may result from confusion with nearby unresolved red or blue secondary components, leading to possible fluctuations in  $\sigma$  across the slit.

In zone 1 (see Fig. 2) an extended, low emission, central valley is surrounded by a broad rim which extends from  $x = 71''$  to  $x = 79''$  between slits 7 to 12. The full dimension of the ring-like structure is  $200$  pc  $\times$   $200$  pc and the H $\alpha$  intensity is a factor of 100 lower in the center or valley region.

The low intensity H $\alpha$  valley is almost coincident with the location of the young stellar cluster derived from the continuum map (Knot A) and is indicated in the figure with large asterisks. The main emission line component is present over the whole area and does not show large velocity variations over zone 1, with a mean value about  $0 \pm 10$  km s $^{-1}$ , with respect to the systemic one.

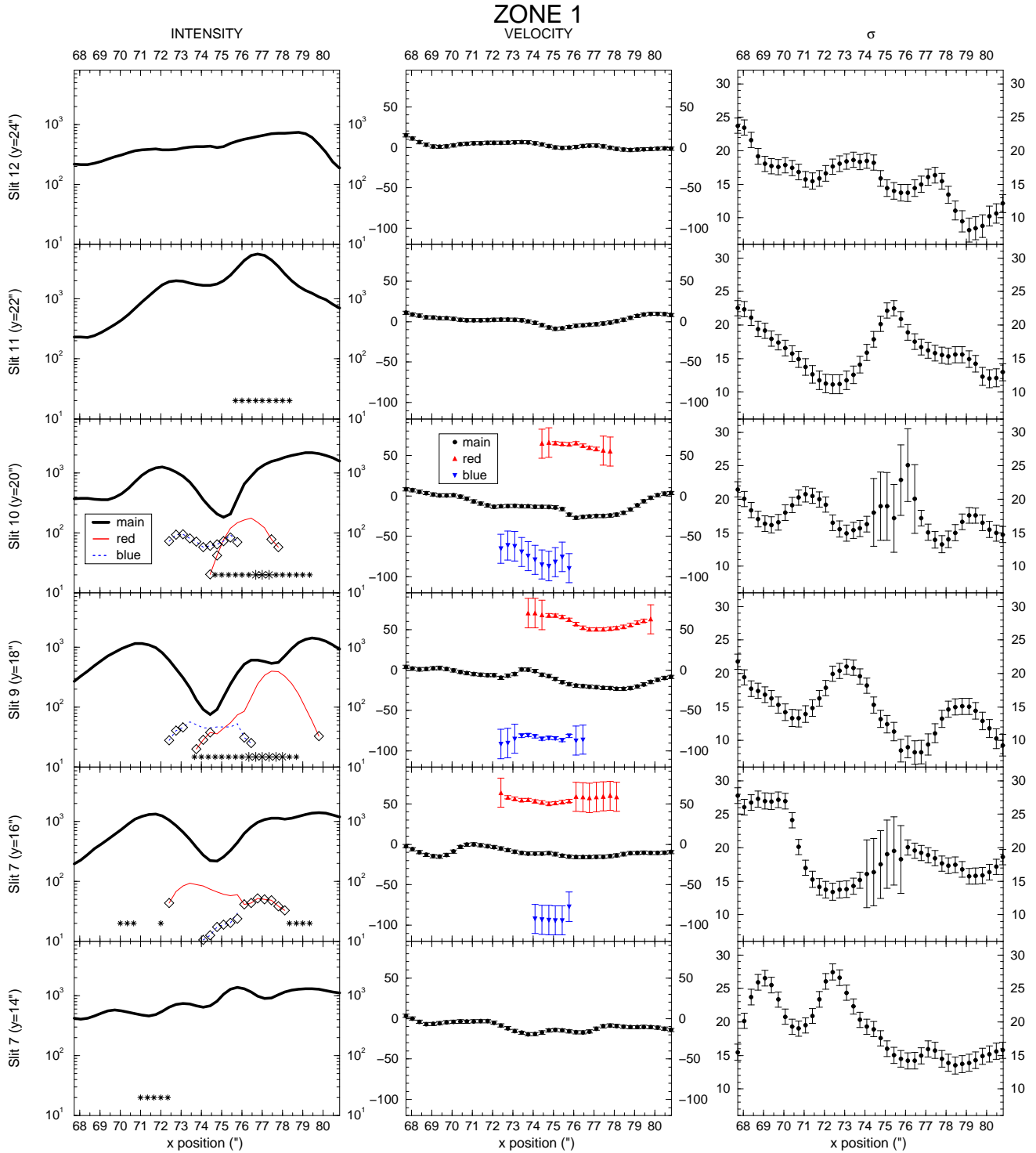


**Fig. 2.** Intensity (first column), velocity (second column) and  $\sigma$  (third column) values fitted to the H $\alpha$  emission corresponding to the spectra of zone 1. In the intensity plots, the thicker line represents the main component. When the red or blue components are detected they are drawn with a thin continuous line (red) or with a thin dashed line (blue). Large asterisks mark continuum knot A while the small ones trace the surrounding extended young population (see Paper I). Diamonds indicate marginal detections as exemplified in Fig. 3. Different symbols are used in the velocity plots to represent the main, blue and red components. The sigma is shown for the main component only. The separation between consecutive slits is  $2''$  (40 pc), and the horizontal scale is in arcseconds ( $1'' = 20$  pc). The units are  $10^{-17}$  erg s $^{-1}$  cm $^{-2}$  arcsec $^{-2}$  for the intensity and km s $^{-1}$  for the velocity and  $\sigma$ .

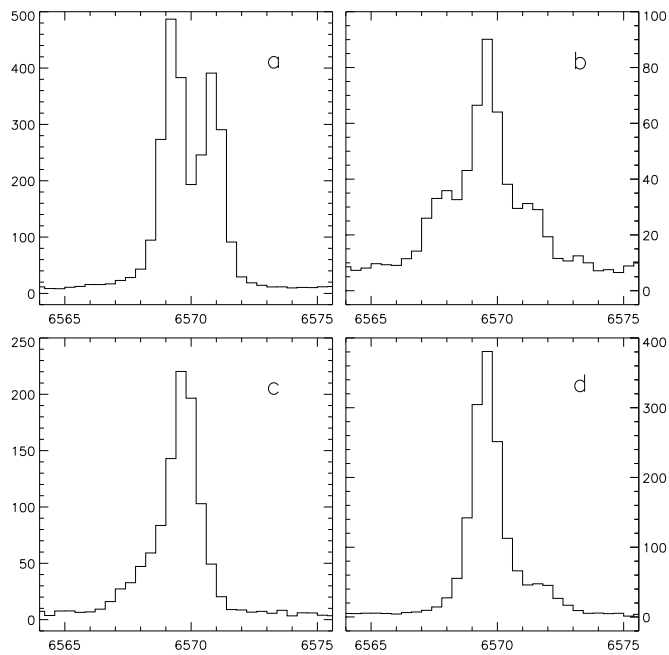


**Fig. 3.** Examples of full and marginal detections. Four spectra taken at different locations along slit 9 are shown. The spectra show well resolved two and three components (a and b) as well as marginal detections (c and d). The units are  $\text{\AA}$  and  $10^{-17} \text{ erg s}^{-1} \text{\AA}^{-1} \text{cm}^{-2} \text{arcsec}^{-2}$  for the  $x$  and  $y$  axes, respectively.

Blue and red secondary components have been detected over an area of about  $140 \text{ pc} \times 120 \text{ pc}$ , extending over the ring-like structure albeit being more evident on the  $\text{H}\alpha$  depression and at the position of the young stellar cluster. The blue and the red secondary line components are displaced by about  $70 \text{ km s}^{-1}$  from the galaxy bulk emission, presenting small velocity variations along the slits ( $\leq 10 \text{ km s}^{-1}$ ).

The velocity width of the main emission line component, ranges from about  $10 \text{ km s}^{-1}$  to  $28 \text{ km s}^{-1}$ . The weighted mean sigma value for the whole zone is supersonic and about  $17 \text{ km s}^{-1}$ . This value is only slightly larger than the integrated one ( $15.0 \pm 0.6 \text{ km s}^{-1}$ ) over the whole NGC 4214-I (zones 1-4) measured by Roy et al. (1986) and Arsenault & Roy (1988).

On the other hand, the NW border of zone 1 traces the edge of the parent cloud, where the line intensity rapidly drops by more than one order of magnitude (as one goes from  $x = 72''$  towards  $x = 68''$ , across slits 8 - 11), and at the same time, the  $\sigma$  value increases steadily to highly supersonic values ( $20$ - $30 \text{ km s}^{-1}$ ) while the velocity line center remains well behaved. An abrupt density drop is necessarily accompanied by a sharp line intensity decrease and if this coincides with the region where the lines become broader, then both observables seem to be tracing a champagne flow (Tenorio-Tagle 1979) playing a major role at the boundary of the ionized cloud.

Although not indicated in Fig 2, a low-level, very wide ( $\sigma \approx 600 - 700 \text{ km s}^{-1}$ )  $\text{H}\alpha$  component was also detected at the location of the young stellar cluster. This very wide com-

ponent was discovered by Sargent & Fillipenko (1991), who attribute its origin to the WR stars known to be present there. Our data corroborates this broad component is centered at the position of the cluster and is not present anywhere else.

### 3.1.2. Zone 2

Fig. 4 shows the results from the detailed analysis of slits 9 - 12 that traverse zone 2. Zone 2 extends from the SE border of zone 1. The main line intensity (thick line on Fig. 4) decreases as one moves towards the SE border of NGC 4214-I. The line intensity falls by almost one order of magnitude from position  $81''$  to  $95''$  on slits 9 to 11, over a distance of up to  $280 \text{ pc}$ , while the peak velocity of this main emission component remains almost constant, at about  $0 \text{ km s}^{-1}$ , the same value measured on zone 1.

Looking at Fig. 4 in further detail one can see that the intensity fall is more pronounced along the first 5 positions (100 pc) on slits 10 and 11. At these coordinates a red secondary component is detected. Since its S/N ratio is not sufficient for a secure fit to be carried out, no  $\sigma$  values are given. The red component velocity however is clearly shifted in a range between  $60$ - $100 \text{ km s}^{-1}$  from the bulk of the  $\text{H}\alpha$  emission. As in Fig. 2 variations in  $\sigma$  might reflect line contamination by non-resolved components affecting the measured line width. It seems that, after reaching the edge of NGC 4214-I, which could be defined at  $x = 86''$ , the ISM is disrupted, most probably by a superposition of two effects: the photoevaporation of the SE edge and the interaction between the two star-forming knots A and B.

### 3.1.3. Zone 3

Zone 3 is traversed by 6 slits (numbers 3 to 8), and includes continuum knot B (see Fig. 5). The  $\text{H}\alpha$  line parameters are shown in Fig. 5. Coincident with the location of this continuum knot (slit 5,  $x = 85$ ), an expanding shell with a velocity of about  $25 \text{ km s}^{-1}$  can be seen. The signature of this shell can be tracked both in the intensity and velocity plots and is one of the few places where a main component cannot be defined, i.e., two components of similar intensity are present at the same time. A spectrum is shown on Fig. 6a. The shell has a radius of  $2.5''$  (50 pc) and is most probably broken as it presents a red dominant component towards its northwestern end and a blue one in the southeastern direction.

As one moves to the right inside zone 3 the  $\text{H}\alpha$  intensity drops by more than an order of magnitude, in a similar way to what happens in zone 2. A large-scale champagne flow has developed. One can also see the signature of a large expanding shell clearly reflected on the intensity and velocity plots (see Fig. 6b) of slit 6. This shell is very elongated and spans almost  $10''$  (200 pc) along the density gradient, but its width is smaller than 40 pc, as it only occurs in one slit. Moving along the slit, the intensities of the red and the blue components add up to similar intensity values displayed by the main component along either slits 5 or 7 at similar locations along the density gradient. The velocity separation implies an expansion of some

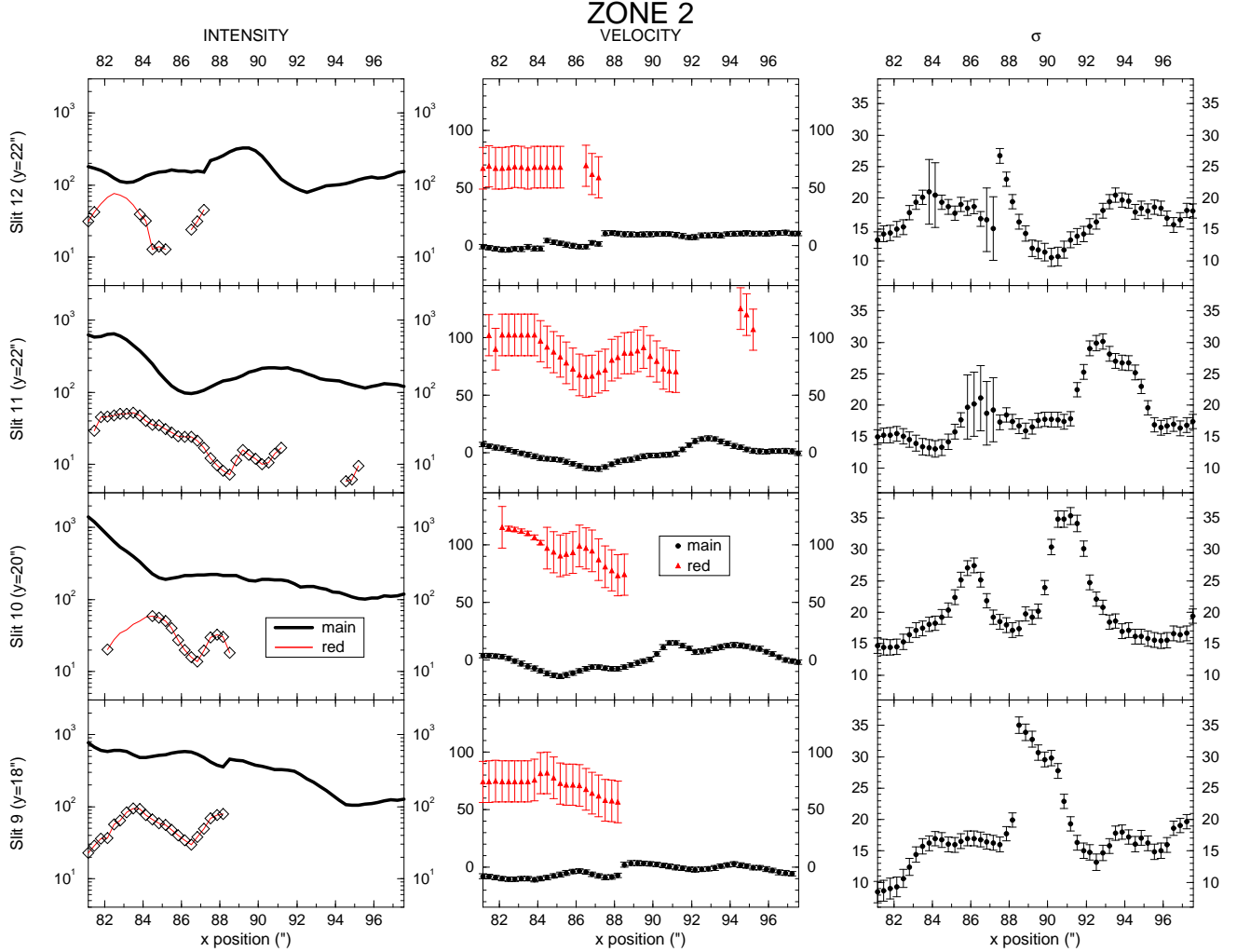


**Fig. 4.** Intensity, velocity and  $\sigma$  values fitted to the H $\alpha$  emission corresponding to the spectra from zone 2. Symbols, lines, slit separation, horizontal scale and units are as in Fig. 2.

25 km s $^{-1}$  (see Fig. 5). The  $\sigma$  trend along the slit can also be understood as resulting from an expanding bubble. Each component, when resolved, has the same line width as that of the gas nearby and at the extreme ends of the slit. The enhancements right at the boundaries of the splitted line region can be understood as the integrated intensity along the line of sight of a thick shell which defines the boundary of the bubble. The width of the two bumps in the  $\sigma$  plot could be taken as a coarse measure of the shell thickness (around 5" or 100 pc).

The second bubble, extended along the density gradient, seems to be spatially connected to the smaller one (sitting on cluster B). Its most likely formation mechanism is a blowout of the first superbubble, produced when evolving into the lower density medium (see Comerón 1997), as we will discuss later.

### 3.1.4. Knot 11

To the NE border of zone 3, though clearly separated, there is a small (about 4" or 80 pc) emission knot (knot 11 on paper I and in Fig. 1). This knot has been analyzed through a slit crossing the peak intensity maximum (slit 2). On each position of the slit, both H $\alpha$  and [O III]  $\lambda 5007$  lines are well fitted by a single Gaussian and the results are shown on Fig. 7.

Both emission lines show similar properties. The physically small but intense emitting knot displays a maximum and almost constant velocity of about 25 km s $^{-1}$  in the case of H $\alpha$  and 35 km s $^{-1}$  in the case of [O III]  $\lambda 5007$  with respect to the systemic one. These velocities imply a redshift of some 25 – 30 km s $^{-1}$  compared to its surroundings. On both sides of the intensity and velocity maxima the lines become broader by more than 10 km s $^{-1}$  with respect to the nearby ISM.

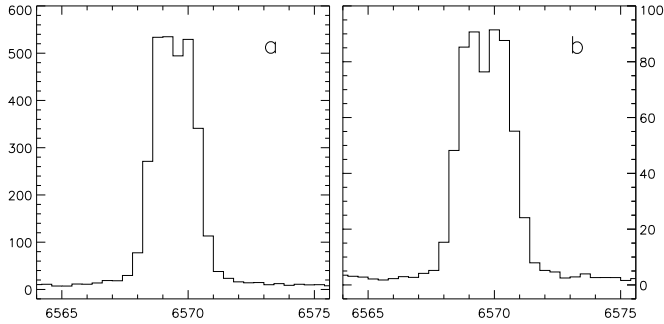


**Fig. 6.** Spectra obtained at the two shells detected on zone 3. The spectrum on the left (a) corresponds to the shell on slit 5 and the one on the right (b) to the one on slit 6. Units are the same as in Fig. 3.

### 3.1.5. Zone 4

Zone 4 represents the NE border (see Fig. 1) of NGC 4214-I and encloses a large area where the emission lines outside the important star-forming regions (clusters A and B) can be analyzed. The zone contains the background ionized medium representative of the intercloud ISM of the galaxy.

As in the other three zones, a plot showing the intensity, velocity and  $\sigma$  fits to the  $\text{H}\alpha$  emission lines has been built and is presented in Fig. 8. The area is covered by 6 slits (slits 1 to 6) and spans from  $x = 59''$  to  $x = 81''$ . Although zone 4 has been chosen to be far from the most intense  $\text{H}\alpha$  knots in zones 1 and 3, their presence can still be traced. As one moves to the southern corner of zone 4 the line intensity progressively increases approaching that measured on zones 1 and 3. Therefore, there is not a sharp boundary at NGC 4214-I as one moves towards the NE on the galaxy, but instead a continuous extended medium all of it with the enhanced values of  $\sigma$  characteristic of the photoevaporation. The velocity of the main component presents values close to the systemic velocity of NGC 4214, as expected, considering the proximity of the area to the main star-forming knots of the galaxy. A few secondary components are detected, including a wide one in slit 6 whose width ( $\sigma \approx 60 \text{ km s}^{-1}$ ) could be measured. However, these components do not seem to possess an organized large scale structure, as suggested by Martin (1998).

In zones 1, 2, 3 and 4, if one takes into account the differences in resolution among the blue and red arms of the spectrograph, the  $[\text{O III}] \lambda 5007$  emission behaves in a very similar way as  $\text{H}\alpha$ . However, the poorer spectral resolution of the spectrograph blue range has inhibited the measurement of the secondary components.

### 3.2. NGC 4214-II (the SE complex)

The ionized gas emission of the star forming complex to the SE has been analyzed through 4 slits starting with slit 9 which crosses the peak emission maxima. At each position on the slit, emission lines are reasonably well described by one sin-

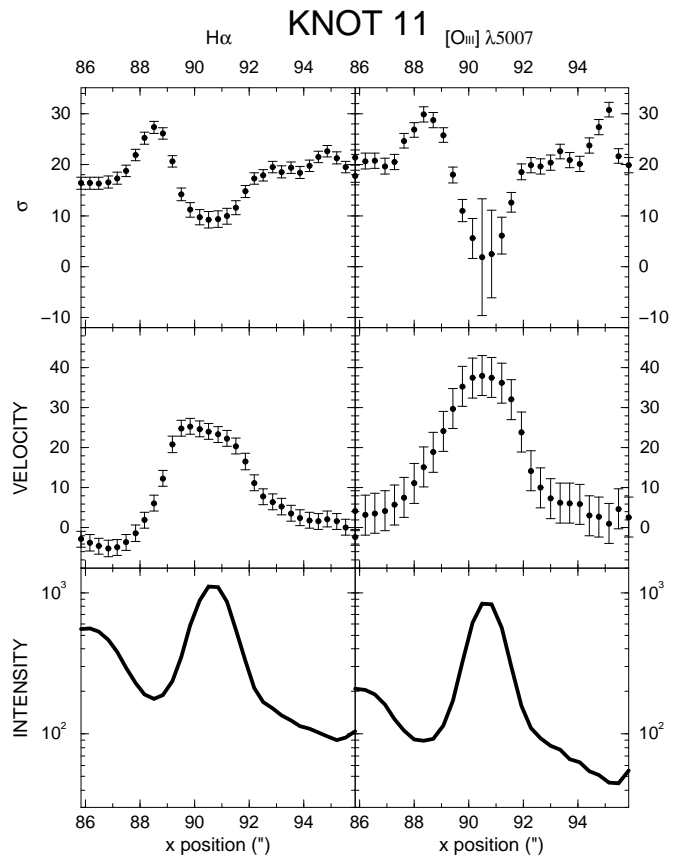


**Fig. 7.** Intensity, velocity and  $\sigma$  values fitted to the  $\text{H}\alpha$  emission and  $[\text{O III}] \lambda 5007$  along the slit crossing knot 11 (slit number 2). Symbols, lines, slit separation, horizontal scale and units are as in Fig. 2.

gle Gaussian and results of the fit of  $\text{H}\alpha$  and  $[\text{O III}] \lambda 5007$  are shown on Figs. 9 and 10. We start the description with slit 9, which will be also taken as the reference for the SE region. The whole complex seems to be blueshifted about 10-20  $\text{km s}^{-1}$  with respect to NGC 4214-I. Within the slit, the velocity spreads on a range of about 15  $\text{km s}^{-1}$ , implying small relative displacements of the ionized gas. The velocity dispersion is around 10  $\text{km s}^{-1}$  and, therefore, sub-sonic almost all over the cloud, except for the left part of the region (from  $x = 98''$  to  $101''$ ). The  $\sigma$  value grows at both borders of the complex, specially at the NW one. On both extremes on the region, the S/N is still good enough for a good fit to be done and artificial broadening of the line due to this reason can be discarded. This possibility of photoevaporation taking place on the borders of the parent cloud implies also a density bounded  $\text{H II}$  region and thus the three intensity peaks could be local density enhancements close to the massive star clusters and presently being disrupted by them. As we move towards the SW edge throughout slits 10, 11 and 12, the intensity decreases and the identity of the individual knots is smeared out. The velocity increases reaching a maximum at position  $x = 98''$  on slit 12.

Line widths also show a tendency to grow and some features showing local maxima both in velocity and in  $\sigma$  can be identified (see e.g., positions from  $102''$  to  $110''$  on slit 12). These again may be features showing gas outflows from the density bounded regions.

### 3.3. The edge of the optical bar and the velocity curve

On the right-hand side of Fig. 1 we display other low intensity features present along the optical bar of the galaxy. Among these, the most evident is the giant ring-like feature between  $x = 145''$  and  $x = 165''$ , with a strong emitting knot (knot 16, in the nomenclature of Paper I). Line widths of both red and blue components increase when reaching the intensity maximum at knot 16. This giant ring could, at first glance, be interpreted as the result of a large energy injection. However, there is no trace of UV continuum associated (Fanelli et al. 1997) and thus no trace of a stellar generation capable of blasting the ISM and causing the 400 pc diameter ring.

Knot 16 has been analyzed by fitting the emission lines along slit 8, which traverses the peak intensity maximum. Results of the  $H\alpha$  fit are shown in Fig. 11. The emission line splits into two components across the knot, and presents a main component an order of magnitude brighter than the background. The velocity of the most intense line reaches a maximum of  $75 \text{ km s}^{-1}$ , compared with the systemic velocity measured in the nearby ISM. The blue line shows a higher relative velocity reaching up to  $-175 \text{ km s}^{-1}$ .

Fig. 12 shows the rotation curve along the  $x$  axis (i.e. parallel to the slits) derived from our data on the central regions of NGC 4214. This was obtained from all the pixels where the main  $H\alpha$  component had a value above a threshold of  $20 \cdot 10^{-17} \text{ erg s}^{-1} \text{ cm}^{-2} \text{ arcsec}^{-2}$ . The threshold was used in order to avoid values with low S/N ratio. Since twelve slits were used, that is the maximum number of points that can appear for a given value of  $x$ .

The central  $90''$  (1.8 kpc) can be reasonably well adjusted by a solid body rotation with a projected velocity gradient of  $18.2 \text{ km s}^{-1} \text{ kpc}^{-1}$  (assuming a distance of 4.1 Mpc). However, some pixels deviate from the mean rotation curve by up to  $30 \text{ km s}^{-1}$ . Three regions show strong deviations towards the blue (around  $x = 77'', 85'',$  and  $101''$ ) and another one towards the red (around  $x = 90''$ ). These regions correspond to continuum knots A and B, and knot E (the NW part of the SE complex) for the blueshifted cases and to knot 11 for the redshifted one. In all cases, they correspond to continuum maxima, indicating that the ionizing stellar clusters can cause peculiar motions in the ionized gas that make them depart from the mean rotation curve determined across the bar.

The velocity curve along the  $x$  direction coincides (within  $5 \text{ km s}^{-1}$ ) along the central 1.8 kpc with the  $H\text{I}$  rotation curve of McIntyre (1998). Although with much lower spatial resolution ( $30''$ ), the  $H\text{I}$  data extends over a much larger area. McIntyre also detected a much larger gradient along the  $y$  direction, which is expected since it corresponds approximately to the minor axis of the galaxy. That effect is not observed in our data.

We attribute it to the short  $y$  range in our data and to McIntyre lower spatial resolution.

Outside the central 1.8 kpc, the rotation curve flattens to the NW and remains approximately constant to the SE. These results are also coherent with those of McIntyre (1998), leading us to conclude that the rotation curves detected in both hydrogen phases are quite similar. The small detected departures can be simply ascribed to random motions induced by the young stellar clusters. A similar conclusion was reached by Hartmann et al. (1986).

## 4. Discussion

The ISM around the nucleus of NGC 4214 is very complex and we do not pretend to offer a complete explanation of its present morphology. There are, however, several features, in particular the largest structures and detected flows, which offer the possibility of assessing the importance of both photoionization and mechanical energy deposition by strong stellar winds and SNe on structuring the ISM.

### 4.1. The ionizing clusters of NGC 4214

We list in Table 1 the observed and derived properties of the massive young ionizing clusters around the nucleus of NGC 4214 and their surrounding shells and bubbles. In our sample we have included the two main ionizing clusters of the NW complex (A and B) and the corresponding three clusters of the SE complex (E, D and K). As mentioned in Paper I, these three clusters are studied together, due to the impossibility of separating them with the available data. We have also included for comparison cluster C. The number of Lyman continuum photons ( $N_{LyC}$ ) has been derived from the luminosity of the  $H\beta$  line. The effective temperature ( $T_{eff}$ ) of each cluster has been obtained from the line ratios given by Kobulnicky & Skillman (1996) following the calibration of Cerviño & Mas-Hesse (1994), as explained in Paper I, except for knot C for which the prediction of the synthesis models has been indicated. The observed radius ( $R^o$ ) and expansion velocity ( $v_{exp}^o$ ) for the superbubble(s) around each cluster are also shown in Table 1. In the case of knot B, the first set of observed values refers to the superbubble centered on the continuum knot while the second set refers to the superbubble located towards the SE of the continuum knot. We also indicate whether a blowout is observed and the measured kinetic energy ( $E_k^o$ ) contained in the observed superbubble assuming that the emitting gas has a density of  $100 \text{ cm}^{-3}$ .

The properties listed in Table 2 have been obtained by combining the observational measurements and derived parameters discussed above and in Paper I with the predictions of evolutionary synthesis starburst models by Cerviño & Mas-Hesse (1994) and Cerviño (1998), according to the following procedure:

- Different parameters ( $W(H\beta)$ , effective temperature, WR stars presence,...) are used to constrain the age ( $t_*$ ) of the ionizing clusters.

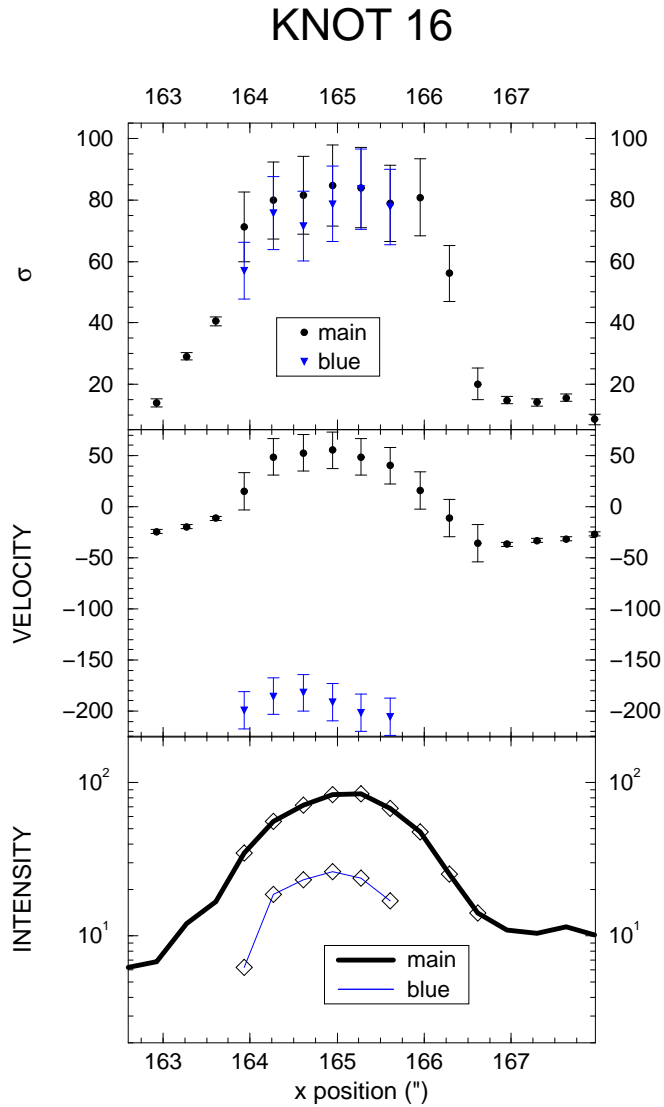


**Fig. 11.** Intensity, velocity and  $\sigma$  values fitted to the H $\alpha$  emission along the slit crossing knot 16. Symbols, lines, slit separation, horizontal scale and units are as in Fig. 2.

- Comparing the total continuum luminosity of each cluster at H $\beta$  with the predictions of the models for the assumed age, we derive the total mass of gas transformed into stars ( $M_*$ ) during the starburst episode. The model predictions are normalized to 1  $M_\odot$  of stars for an instantaneous burst with a Salpeter Initial Mass Function between 2 and 120  $M_\odot$ . We have extrapolated the derived mass of the clusters given in Table 2 to the range 0.1 to 120  $M_\odot$ .
- The model predictions for the mechanical energy input rate (due to stellar winds and supernovae) and the total release of mechanical energy during the history of the cluster ( $L_k$  and  $E_k$  respectively) are de-normalized by the total mass of the cluster at the given age.

- Following Bodenheimer et al. (1979) we have finally computed the kinetic energy given to the gas upon photoionization during the champagne phase as

$$E_{photo} = fkT_{eff}N_{Ly\alpha} \quad (2)$$

where  $f$  represents a correction factor that accounts for the fraction of the photon energy that remains as heat and the energy radiated away and for the fact that when the starburst is younger a higher number of ionizing photons are emitted. From the data given in Table 1 and assuming  $f \sim 0.1$  (a somewhat arbitrary value), we derived the  $E_{photo}$  values given in Table 2.

#### 4.2. The giant H II regions in NGC 4214

The main characteristic of giant H II regions is their supersonic line width ( $15 \text{ km s}^{-1} \leq \sigma \leq 40 \text{ km s}^{-1}$ ), believed to be related to the ionizing cluster formation stage (see Tenorio-Tagle et al. 1993). The action of stellar winds and supernova explosions could also contribute to broaden the emission lines but, since the  $\sigma$  values correlate with the size of the emitting regions, as shown by Terlevich & Melnick (1981), the main driver seems to be related to the original properties of the protocluster. Perhaps the best criterium to select the size of a giant H II region is through a determination of the “kinematic core” (Muñoz-Tuñón et al., 1995). This is the size of the area of the ionized nebula across which a single Gaussian supersonic line can be found. Good examples of this are the giant H II regions of M101 (Muñoz-Tuñón 1994) and those catalogued in NGC 4449 (Fuentes-Masip 1997).

NGC 4214-I presents supersonic emission line widths and has previously been classified as a single giant H II region. Arsenault & Roy (1988), for example, list it as a region 560 pc in diameter with an e-folding velocity width of  $21.1 \text{ km s}^{-1}$ . Our studies, however, (see Section 2 and Paper I) have clearly shown that two well separated and massive young clusters contribute to the ionization of NGC 4214-I (cluster A in zone 1 and B in zone 3). The presence of two stellar clusters implies that NGC 4214-I may not be a single giant H II region but rather the result of two neighbouring ones. Under such assumption one can infer dimensions and velocity dispersion values for the two H II regions from our high resolution data. The H II region around cluster A has a radius comparable to the distance between the cluster and the western edge of the dense region, which presents the largest intensity and a supersonic  $\sigma$  value ( $\sigma = 17 \text{ km s}^{-1}$ ). This radius is equal to 100 pc. Note that this also coincides with the cluster radius derived from HST data by Leitherer et al. (1996). The region around cluster B seems to be more distorted by the mechanical energy deposited by the massive stars. This H II region shows a central superbubble and a secondary larger bubble extending along the edge of the cloud. However, a radius and a  $\sigma$  value can be obtained from the values of the still mechanically unperturbed regions, or area exterior to the central shell. When doing so we obtain values of  $R = 100 \text{ pc}$  and  $\sigma = 20 \text{ km s}^{-1}$ . Although it is clear that the uncertainties in the parameters associated to the two H II regions

**Table 1.** Observed and derived properties of the stellar clusters in NGC 4214 and their surrounding bubbles.

| Knot  | $N_{Ly\alpha}$<br>$10^{51} \text{ s}^{-1}$ | $T_{eff}$<br>$10^3 \text{ K}$ | $R^o$<br>pc     | $v_{exp}^o$<br>$\text{km s}^{-1}$ | blowout | $E_k^o$<br>$10^{50} \text{ erg}$ |
|-------|--------------------------------------------|-------------------------------|-----------------|-----------------------------------|---------|----------------------------------|
| A     | 4.5                                        | 37.0                          | 100             | 70                                | YES     | 1.0                              |
| B     | 1.8                                        | 37.0                          | 50              | 25                                | NO      | 0.9                              |
|       |                                            |                               | 200 $\times$ 40 | 25                                | YES     | 0.6                              |
| C     | 0.42                                       | 34.0                          | 70?             |                                   | YES     |                                  |
| E+D+K | 4.4                                        | 38.5                          | < 10            |                                   | NO      |                                  |

are very large, the important result is to resolve the complex NGC 4214-I into two separate GHIIRs. This new classification makes both of them fall on the Terlevich & Melnick (1981)  $R$  vs.  $\sigma$  and  $L(H\beta)$  vs.  $\sigma$  correlations. On the other hand, if we consider both as a single entity, the resulting region does not fall on the correlation.

The large H II region NGC 4214-II does not present a uniform supersonic line width and, therefore, does not belong to the giant H II region class.

#### 4.3. Shells, bubbles, superbubbles

We have presented kinematical evidence of the existence of three shells in NGC 4214-I, one of them associated to the most massive starburst (cluster A in zone 1) and two more some 400 pc to the south (associated to cluster B in zone 3). There is also a broken large-scale ring-like low intensity feature (see Fig. 1,  $x = 145''$  to  $170''$ ) located 1.8 kpc away from the nucleus.

Given the mechanical energy expected from the ionizing massive clusters and their age, one can attempt to derive the properties of the superbubbles (radius  $R$ , expansion speed  $v_{exp}$ , kinetic energy  $E_k$ ) that they should have produced, assuming a uniform mass density  $\rho_0$  for the background medium. This was done by Weaver et al. (1977) assuming a constant mechanical energy input rate  $L_k$ . However, that hypothesis is not valid for a starburst. During the first 3 Myr after the formation of the cluster, the mechanical energy input is dominated by winds from early type O stars. These stars present an increasing wind luminosity with time. This effect can be clearly seen in Fig. 13, where the mechanical energy input rate and integrated value (obtained from the models of Cerviño & Mas-Hesse (1994) and Cerviño (1998)) as a function of time have been plotted. Although the model of Weaver et al. (1977) is therefore not directly applicable, an analytical solution can still be found, as shown in the Appendix, yielding:

$$R(\text{kpc}) = 0.88 \left( \frac{L_{41}}{n_0} \right)^{\frac{1}{5}} t_7^{\frac{3}{5}} \quad (3)$$

$$v_{exp}(\text{km s}^{-1}) = 52 \left( \frac{L_{41}}{n_0} \right)^{\frac{1}{5}} t_7^{-\frac{2}{5}}, \quad (4)$$

where  $L_{41}$  is the present luminosity in units of  $10^{41} \text{ erg s}^{-1}$  (not constant any more),  $n_0$  is the background gas density in  $\text{cm}^{-3}$ , and  $t_7$  is the evolution time in units of  $10^7 \text{ yr}$ . This model has, of course, its limitations: As it can be seen in Fig. 13, a

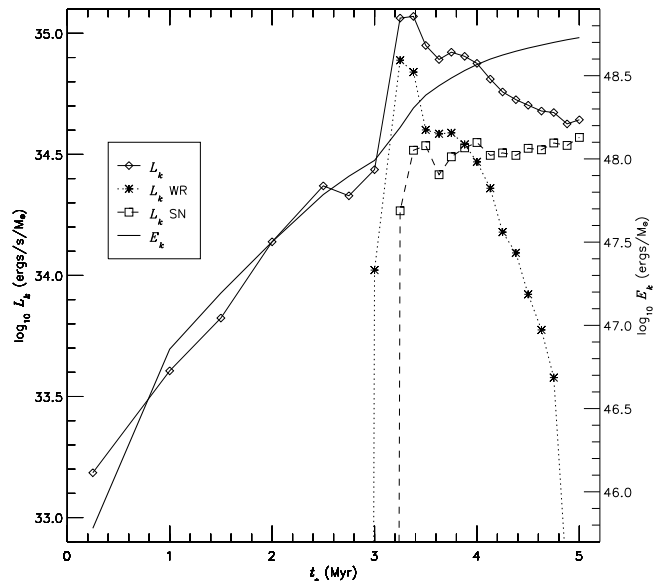


**Fig. 13.** Mechanical energy input rate ( $L_k$ ) and integrated value ( $E_k$ ) per unit mass as a function of time for an instantaneous burst with  $Z = 0.008$  (which is close to the metallicity of NGC 4214, see Kobulnicky & Skillman (1996)) and a Salpeter IMF between 2 and  $120 M_\odot$ .  $L_k$  is the sum of the contribution from winds from non-Wolf-Rayet stars, winds from Wolf-Rayet stars and supernovae. The contribution to  $L_k$  from Wolf-Rayet winds and supernovae has also been represented.

power law cannot provide a good fit over periods of time longer than 3–4 Myr. However, it can always serve as a comparison to the constant input rate model of Weaver et al. (1977) in order to provide an estimate of the dependence of  $R$  and  $v_{exp}$  on the variability of the mechanical energy input rate.

Applying Eqs. 3 and 4 to the derived data of the different regions we have obtained the size and expansion velocities of the expected superbubbles. The results appear in Table 2, where a background density of  $100 \text{ cm}^{-3}$  has been assumed (see Paper I). These superbubble parameter predictions have to be taken with caution when compared with the observational values. They would correspond to the properties that the bubbles and shells should have assuming spherical symmetry and an homogeneous interstellar medium.

**Table 2.** Some properties of the clusters and superbubbles in NGC 4214 obtained from the synthesis models, as explained in the text. The assumed background density is  $100 \text{ cm}^{-3}$ .  $M_*$  is normalized to the range  $0.1 - 120 \text{ M}_\odot$  assuming a Salpeter IMF (note that this normalization is different from the one applied in Fig. 13).  $R^t$  and  $v_{exp}^t$  have been calculated from Eqs. 3 and 4. However, since C is older than around 3.5 Myr, we have included not only the predictions of Eqs. 3 and 4 but also those from Eqs. .11 and .12.

| Knot  | $M_*$<br>$10^5 \text{ M}_\odot$ | $t_*$<br>Myr | $R^t$<br>pc | $v_{exp}^t$<br>$\text{km s}^{-1}$ | $L_k$<br>$10^{39} \text{ erg s}^{-1}$ | $E_k$<br>$10^{51} \text{ erg}$ | $E_{photo}$<br>$10^{51} \text{ erg}$ |
|-------|---------------------------------|--------------|-------------|-----------------------------------|---------------------------------------|--------------------------------|--------------------------------------|
| A     | 3.5                             | 3.0-3.5      | 116         | 21                                | 11.6                                  | 155                            | 236                                  |
| B     | 1.0                             | 3.0-3.5      | 91          | 17                                | 3.5                                   | 46                             | 94                                   |
| C     | 0.7                             | 3.5-4.5      | 87-110      | 13-16                             | 1.5                                   | 74                             | 27                                   |
| E+D+K | 1.6                             | 2.8-3.3      | 70          | 14                                | 1.2                                   | 44                             | 213                                  |

Around cluster A one can see the main emission from the galaxy across the low intensity valley but not a complete shell of 116 pc across expanding with a velocity of  $21 \text{ km s}^{-1}$  as expected from the theory (see Table 2). The lack of a large kinematically detected shell around cluster A thus implies a limiting mechanism or a threshold value in the galaxy that inhibits the build up of structures larger than about 100 pc in radius, implying the blowout of the superbubble. On the other hand, there is a ring-like feature associated to the starburst located at the UV nucleus (see Section 3.1.1), which presents a red and a blue component in  $\text{H}\alpha$  at various positions across it. Both components are shifted some 70 km s $^{-1}$  from the main most intense line placed at a velocity  $\sim v_{\text{galaxy}}$ . The presence of this main component implies that the stellar activity, even in the nucleus of the galaxy, has not been efficient enough to sweep all the surrounding ISM into a shell. The shell-like structure is really a depression found in the intensity of the various lines but it is not a cavity as that predicted by theoretical models of stellar winds and SN remnants. Furthermore, in a velocity vs. position diagram the feature does not present the characteristics typical of an expanding shell (such as the largest splitting when observed towards the center and a single emission line nearer the edge) and the observed  $v_{exp}$  is much larger than the expected value. The feature, apart from the strongest emission centered at the velocity of the galaxy, presents an extended red component spatially shifted from the less extended blue counterpart. The only geometry in agreement with all these features is that of a young filled superbubble bursting out on both sides of an almost face-on and thin galaxy disk and undergoing a sort of jet-like process (Comerón 1997). Lines of sight across the bubble will display first the blue component (from the bursting counterpart approaching us) and then a region of overlap between the blue and the (now unobsured by the disk) red component. The latter will extend even further than the blue one when lines of sight begin to pick up the part of the shell that is bursting out of the disk on our side but whose furthest away side is expanding away from us.

The superbubble expected around the star cluster B also seems to have burst out of the parent cloud but this time into the intercloud medium causing an elongated and larger secondary shell, both of them well detected in our spectra (see Fig. 5). The expanding shells are still detected; the first one has experienced blowout whereas the second one is still complete and,

therefore, does not seem to have experienced blowout yet. It is interesting to note that the expansion velocity expected is roughly consistent with the observational value, despite the irregular geometry induced by the blowout of the main shell.

The above discussion is in agreement with recent observations reported by Martin (1998) who finds evidences of shells and loops structures out of the main optical body of NGC 4214. She finds no peculiar kinematical patterns associated to them. This, together with the known fact that blowout has already taken place on present day starbursts, points towards the presence of secondary shells generated by sweeping an extended component of the  $\text{H}\text{I}$  halo material.

For the three clusters in the SE complex (the youngest star-forming region in NGC 4214), we find no peculiar kinematical features –except for the champagne flows at the borders–, while from their evolutionary state and associated energetics we would expect to find an  $R \approx 70 \text{ pc}$  superbubble at low expansion velocity ( $\approx 14 \text{ km s}^{-1}$ , see Table 2). This disagreement cannot be solved by assuming the existence of three smaller unresolved bubbles around clusters E, D and K, since the expected radius in that case would be around 60 pc for each one of them and should appear resolved in our data.

One possible explanation to this apparent lack of a superbubble is the existence of a strong density gradient. Such a gradient would have led to a blowout as described by Comerón (1997), similar to the one in the NW complex. However, such a blowout should have produced effects which are not observed in the SE complex: the maximum of the gas emission is not shifted with respect to the continuum (as it is in the NW complex) and the  $\text{H}\alpha$  profile does not deviate from a gaussian profile within the accuracy of our data. Comerón (1997) predicts that asymmetries in the  $\text{H}\alpha$  profile should appear at a level of  $\approx 0.03 - 0.05$  times the maximum intensity and we do not find them even at a level 10 times lower. Therefore, the most likely explanation for the non-detection of a superbubble in this region is its real absence. A similar result is obtained for a small cluster in NGC 604 which is apparently younger than the rest of the recently formed stars there (Maíz-Apellániz et al. 1999).

What other possibilities can explain the non-existence of this superbubble in the SE complex? We postulate that the origin is the existence of an inhibiting mechanism for the creation of superbubbles by winds during the first 2-3 Myr after the formation of the starburst. If we delay the onset of the formation

of the superbubble for such a period of time, both the non-detection of a superbubble in the SE complex and the small size of the ones detected in the NW complex could be explained. This delay with respect to the theoretical predictions could be associated to the results of Bernasconi & Maeder (1996). Their calculations show that very massive ( $> 60 M_{\odot}$ ) stars take 2 to 2.5 Myr to accrete their mass and that during that period of time they are already burning hydrogen while hidden inside their high density molecular gas cocoons. Therefore, the release of mechanical energy by the most massive stars during the first 2 Myr after the onset of a burst would be much smaller than expected, and so the formation of bubbles and shells would not really start until the most massive stars have completed their accretion processes, at a burst age of around 2 Myr. We note here that due to this effect the  $W(H\beta)$  values predicted by present evolutionary synthesis models, which assume all stars at ZAMS at the same time, would be significantly overestimated. This could explain the lack of detection of starbursts with  $W(H\beta)$  values above 300 Å, while synthesis models predict values for young bursts well above 500 Å.

Based on these results, we propose that NGC 4214 is a dwarf spiral galaxy, with a disk much thinner than that of other irregulars with similar optical appearance like, for example, NGC 4449 or NGC 2363. In this way all the structures produced by the stellar mechanical energy input must become disrupted after blowout, as soon as their remnants exceed the small thickness of the galactic disk ( $\sim 200$  pc). Once this happens and given the orientation of the galaxy, there should remain no clear kinematical information to be detected in the optical regime. In such a case, it is only the morphological detection of elongated rings, loops and holes that can provide us with some idea about the power of the stellar energy input. On the other hand, in irregular galaxies such as in NGC 4449, NGC 2366 or Ho II, with an ISM distributed into a much thicker disk, shell structures can be larger, more massive, and longer lived. In such a case remnants of the stellar activity are more easily recognizable not only through their morphology but also kinematically by means of well detected line splitting. According to this scenario, the lack of well defined structures would not be surprising when comparing NGC 4214 with, for example, NGC 4449 (Fuentes-Masip et al. 1995) or with NGC 1569 (Tomita et al. 1994) for which similar studies of the central 2 kpc with comparable, or even poorer, resolution have yielded a large number of kinematical features and thus to what at first glance may seem a richer structure of the ISM.

This scenario would also be consistent with the overestimation by evolutionary synthesis models of the total mechanical energy released, as it is clear from Tables 1 and 2 when comparing the predicted and the measured values. First of all, the delay in the apparition of the most massive stars would significantly reduce the total release of mechanical energy compared with the prediction of synthesis models. Furthermore, the disruption of the structures discussed above inhibits the measurement of the kinetic energy of the gas in the optical regime. And, finally, an important fraction of the mechanical energy should have contributed to heat the interstellar gas, which would cool

by the diffuse X-ray emission detected in these galaxies, as discussed in Cerviño (1998).

The only large-scale ring structure detected is the one at 1.8 kpc from the nucleus. As already discussed on Sect. 3 it is unlikely that the structure had been generated by present day star formation. It is most surely produced by the general UV background of the galaxy. The feature is also identified in the H I maps of McIntyre (1998), where it presents also a ring-like shape around a central depression. It therefore seems very likely that the feature results from the partial ionization of the H I ring bordering the disrupted and yet undetected giant molecular cloud being eroded by the background UV flux. The giant cloud would sit at the end of the bar where matter accumulation is probably leading to the build up of clouds. In such a scenario, the giant cloud is thus predicted to fill the central depression seen in the H I distribution.

#### 4.4. Photoionization champagne flows and froth features

NGC 4214-I might be density bounded, according to Leitherer et al. (1996) and Sargent and Filippenko (1991). We found in Paper I that most of the Lyman continuum photons produced by the young stellar clusters were ionizing the dense gas clouds located to the south of them. The inhomogeneous distribution of gas suggests that some fraction of these photons might be leaking from the star-forming regions. This might also be the case for all the H II regions in the SE complex. Along the borders of all of them, sharp line intensity drops of more than an order of magnitude are accompanied by a sudden increase in the gas velocity dispersion up to supersonic speeds.

Both of these flow features agree with the predictions from the champagne phase (Tenorio-Tagle 1979). UV photons leaking out of a dense cloud into the surrounding medium generate upon photoionization a large pressure difference causing the champagne flow and with it the dispersal of the dense cloud. Therefore, density bounded H II regions here and in any other galaxy must display larger values of  $\sigma$  across their borders, being this  $\sigma$  value provided by the matter expelled at supersonic speeds from the ionized cloud into the background during this champagne phase. Following Bodenheimer et al. (1979) one can calculate the kinetic energy given to the gas upon photoionization during the champagne phase by Eq. 2. As explained above, we have assumed  $f \approx 0.1$ , but this value could be smaller if some of the UV photons are not absorbed across the champagne flows and escape the main disk of the galaxy. In any case, the values of  $E_{photo}$  listed in Table 2 would be sufficient to justify the large  $\sigma$  values observed at the edges of all ionized clouds.

The implication of such energetics has a great impact on the parent clouds which might become disrupted in a time scale of the order of a few times the crossing time ( $t_{ch} \sim \text{cloud size}/ac_{\text{H II}}$ , where  $c_{\text{H II}}$  is the speed of sound for an H II region and  $a$  is a small number in the range 3 to 5).

In NGC 4214-II the outflow can be traced some 200 pc away from the sharp intensity (density) discontinuity and covers the region where Hunter & Gallagher (1990) detected some

“froth” features. The outflow away from NGC 4214-I presents much larger velocities and thus it is very likely that a large fraction of the energy of the nuclear starburst is presently being vented into the halo of the galaxy. All of these features in the SE and NW complexes, together with the size of the main superbubble point at a very narrow galaxy disk of at most 200 pc across. The disk is presently being extended or lifted through champagne flows causing a diffuse broad (200 pc) layer on top of the main galaxy disk. The interaction of neighbouring champagne flows would likely lead to sharp, and more intense regions at the planes of interaction that could more easily be detected and we believe could then be recognized as froth.

We thus conclude that the mechanical input deposited by the star formation complexes, in a variety of physical processes that include the free expanding bubbles liberated after blowout and photoevaporation of the parent clouds, have succeeded in generating structures now detected far from the disk. The latter also supports the presence of and extended H I halo, sometimes partly ionized and seen as the DIG of the galaxy. The impact of starbursts gives place to the large-scale structure which now enriches the optical appearance of the galaxy.

## 5. Conclusions

We have analyzed the kinematical properties of the ionized gas around the massive star clusters in the nucleus of NGC 4214 which were studied in Paper I. The main results we have obtained can be summarized as follows:

- Emission lines splitted into several components, as well as significant variations of the line widths, have been detected in several places.
- The Giant H II region around the two most massive clusters in NGC 4214 (A and B) is resolved into two clearly separated regions, each one of them associated to one of the clusters. Both H II regions taken separately fall on the Terlevich & Melnick (1981)  $R$  vs.  $\sigma$  and  $L(H\beta)$  vs.  $\sigma$  correlations. On the other hand, if they are taken as a single region they do not fall on the correlations.
- There are several other young star clusters (C, D, E and K among them) which are not massive enough to produce a Giant H II region around them. Instead, the result is a regular H II region.
- We have not detected superbubbles with the properties that would be expected according to the evolutionary state of the stellar clusters. Around cluster A, only a ring-like feature with three kinematical components at various positions has been identified. Around cluster B, two expanding shells have been identified; the first one seems to have experienced blowout, whereas the second one is still complete. No kinematical features indicating the presence of shells and bubbles have been found around the clusters of the SE complex. These results are in agreement with the Bernasconi & Maeder (1996) model, in which massive stars spend their first 2-3 Myr inside their cocoons.
- We postulate that NGC 4214 is a dwarf spiral galaxy, with a thin ( $\sim 200$  pc) disk that inhibits the formation of large

scale structures in the ISM, which should have been disrupted after blowout, as soon as their remnants exceed the galactic disk.

- Champagne flows might have formed at the borders of the regions, especially on the SE complex, explaining the existence of the diffuse ionized gas around the galaxy.

*Acknowledgements.* The authors would like to thank the referee, C. Robert, for her useful advice on how to improve this paper. JMA would like to acknowledge the hospitality of the Instituto de Astrofísica de Canarias and the Royal Greenwich Observatory, where part of this work has been carried out. This work is based on observations taken with the William Herschel Telescope at El Roque de los Muchachos Observatory located on the island of La Palma. The observations were obtained within the GEFE (*Grupo de Estudios de Formación Estelar*) collaboration, an international group whose main objective is the understanding of the parameters that control massive star formation in starbursts. This work has been partially supported by DGICYT grant PB94-1106, by CICYT grant ESP95-0389-C02-02, and by the IAC.

## References

Arsenault, R., Roy, J.-R., 1988, A&A, 201, 199  
 Bodenheimer, P., Tenorio-Tagle, G., Yorke, H. W., 1979, ApJ, 233, 85  
 Bernasconi, P. A., Maeder, A., 1996, A&A, 307, 829  
 Cerviño M., Mas-Hesse J. M., 1994, A&A, 284, 789  
 Cerviño M., 1998, PhD thesis, Universidad Complutense, Madrid  
 Comerón, F., 1997, A&A, 326, 1195  
 Fanelli, M. N. et al. 1997, ApJ, 481, 735  
 Fuentes-Masip, O., Castañeda, H. O., Muñoz-Tuñón, C., 1995, A.S. P. Conference Series, 71, 143.  
 Fuentes-Masip, O., 1997, PhD., Universidad de La Laguna  
 Hartmann L.W., Geller M.J., Huchra J. P., 1986, AJ, 92, 1278  
 Hunter, D. A., Gallagher, J. S. III, 1990, ApJ, 362, 480  
 Kobulnicky, H. A., Skillman, E. D., 1996, ApJ, 471, 211  
 Leitherer C., Vacca, W., Conti, P. S., Filippenko A. V., Robert C., Sargent W. L. W., 1996, ApJ, 465, 717  
 Maíz-Apellániz, J., Mas-Hesse, J. M., Muñoz-Tuñón, C., Vílchez, J. M., Castañeda, H. O., 1998, A&A, 329, 409 (Paper I)  
 Maíz-Apellániz, J. et al. , 1999, in preparation  
 Martin, C.L., 1998, ApJ, in press.  
 McIntyre, V. J., 1998, PASA, 15, 157.  
 Muñoz-Tuñón, C., 1994, in *Violent Star Formation: From 30 Doradus to QSOs*, ed. G. Tenorio-Tagle, Cambridge University Press, 25  
 Muñoz-Tuñón, C., Gavryusev, V., Castañeda, H. O., 1995, AJ, 110, 1630  
 Muñoz-Tuñón, C., Fuentes-Masip, O., Castañeda, H. O., 1998, PASA, 15, 103.  
 Roy, J.-R., Arsenault, R., Joncas, G., 1986, ApJ, 300, 624  
 Sandage A., Bedke J. 1985, AJ, 90, 1992  
 Sargent, W. L. W., Filippenko, A. V., 1991, AJ, 102, 107  
 Tenorio-Tagle, G., 1979, A&A, 71, 59  
 Tenorio-Tagle, G., Muñoz-Tuñón, C., Cox, D. P., 1993, ApJ, 418, 767  
 Tenorio-Tagle, G., Muñoz-Tuñón, C., Pérez, E., Melnick, J., 1997, ApJ, 490, L179.  
 Terlevich, R., Melnick, J., 1981, MNRAS, 195, 839  
 Tomita, A., Ohta, K., Saito, M., 1994, PASJ, 46, 335  
 Weaver, R. et al. , 1977, ApJ, 218, 377.

## Appendix

In this appendix we discuss an analytical solution for the expansion of an adiabatic wind-driven bubble in a uniform background medium with mass density  $\rho_0$ . Weaver et al. (1977) developed a model for the case where the bubble was powered by a single star with constant mechanical energy input rate  $L_k$ . In that case, if  $E$  is the internal energy,  $R$  is the radius of the bubble and  $p$  is the pressure, the equations to be applied (the ideal gas equation of state and the momentum and energy balance equations) can be expressed as:

$$E = 2\pi R^3 p \quad (5)$$

$$\frac{d}{dt} \left( R^3 \rho_0 \frac{dR}{dt} \right) = 3R^2 p \quad (6)$$

$$\frac{dE}{dt} = L_k - 4\pi R^2 p \frac{dR}{dt}. \quad (7)$$

The above equations have an analytical solution which can be expressed as:

$$E = \frac{5}{11} L_k t \quad (8)$$

$$R = \left( \frac{250}{308\pi} \right)^{\frac{1}{5}} L_k^{\frac{1}{5}} \rho_0^{-\frac{1}{5}} t^{\frac{3}{5}} \quad (9)$$

$$p = \frac{7}{(3850\pi)^{\frac{2}{5}}} L_k^{\frac{2}{5}} \rho_0^{\frac{3}{5}} t^{-\frac{4}{5}}. \quad (10)$$

Here we are interested in the evolution of two kinematical quantities:  $R$  and the expansion velocity  $v_{exp} = \frac{dR}{dt}$ . In more convenient units, those are:

$$R(\text{kpc}) = 1.1 \left( \frac{L_{41}}{n_0} \right)^{\frac{1}{5}} t_7^{\frac{3}{5}} \quad (11)$$

$$v_{exp}(\text{km s}^{-1}) = 66 \left( \frac{L_{41}}{n_0} \right)^{\frac{1}{5}} t_7^{-\frac{2}{5}} \quad (12)$$

where  $L_{41} = L_k/10^{41} \text{erg s}^{-1}$ ,  $t_7$  is the evolution time in units of  $10^7 \text{yr}$  and  $n_0$  is the density of the background gas in  $\text{cm}^{-3}$ .

The solution to be developed here has a power-law dependence for the mechanical energy input rate  $L_k = At^\alpha$ , where  $A$  and  $\alpha$  are constants. In that case, Eqs. .5, .6 and .7 can still be solved analytically, the result being:

$$E = \frac{5}{11+3\alpha} At^{1+\alpha} = \frac{5}{11+3\alpha} L_k t \quad (13)$$

$$\begin{aligned} R &= \left( \frac{375}{2\pi(3+\alpha)(7+4\alpha)(11+3\alpha)} \right)^{\frac{1}{5}} A^{\frac{1}{5}} \rho_0^{-\frac{1}{5}} t^{\frac{3+\alpha}{5}} \\ &= \left( \frac{375}{2\pi(3+\alpha)(7+4\alpha)(11+3\alpha)} \right)^{\frac{1}{5}} L_k^{\frac{1}{5}} \rho_0^{-\frac{1}{5}} t^{\frac{3}{5}} \end{aligned} \quad (14)$$

$$\begin{aligned} p &= \left( \frac{(3+\alpha)^3 (7+4\alpha)^3}{67500\pi^2 (11+3\alpha)^2} \right)^{\frac{1}{5}} A^{\frac{2}{5}} \rho_0^{\frac{3}{5}} t^{\frac{2\alpha-4}{5}} \\ &= \left( \frac{(3+\alpha)^3 (7+4\alpha)^3}{67500\pi^2 (11+3\alpha)^2} \right)^{\frac{1}{5}} L_k^{\frac{2}{5}} \rho_0^{\frac{3}{5}} t^{-\frac{4}{5}}. \end{aligned} \quad (15)$$

As it can be seen, when the radius is expressed as a function of the present luminosity  $L_k$ , the only difference between Eqs. .9 and .14 is the constant which multiplies  $L_k^{\frac{1}{5}} \rho_0^{-\frac{1}{5}} t^{\frac{3}{5}}$ .

Applying a least-squares fit to the evolution of the mechanical energy input with time (see Fig. 13), it can be seen that  $L_k$  can be reasonably well adjusted by a power law during the first three million years after the formation of the starburst. The best fit yields  $\alpha = 1.25$ . In that case, the constant in Eq. .14 is lower by a factor of 0.79 than the one in Eq. .9. Therefore, for the case  $\alpha = 1.25$  we have:

$$R(\text{kpc}) = 0.88 \left( \frac{L_{41}}{n_0} \right)^{\frac{1}{5}} t_7^{\frac{3}{5}} \quad (16)$$

$$v_{exp}(\text{km s}^{-1}) = 52 \left( \frac{L_{41}}{n_0} \right)^{\frac{1}{5}} t_7^{-\frac{2}{5}}. \quad (17)$$

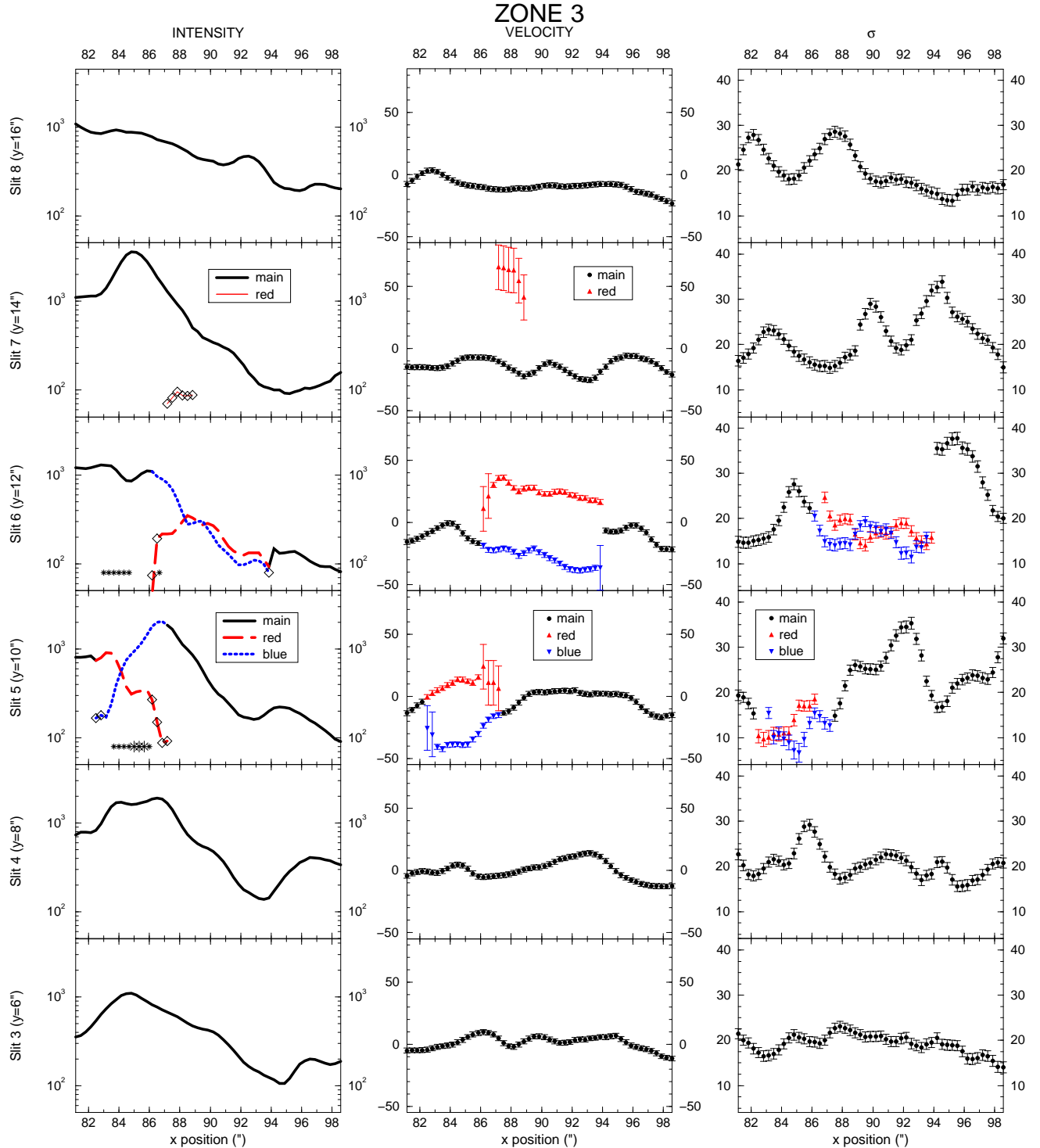


**Fig. 5.** Intensity, velocity and  $\sigma$  values fitted to the H $\alpha$  emission corresponding to the spectra from zone 3. Symbols, lines, slit separation, horizontal scale and units are as in Fig. 2. Asterisks correspond to continuum knot B. When two components are present and it is not possible to decide which one is the main one, both are represented with a thick line. In these cases, where possible,  $\sigma$  is shown for both components.

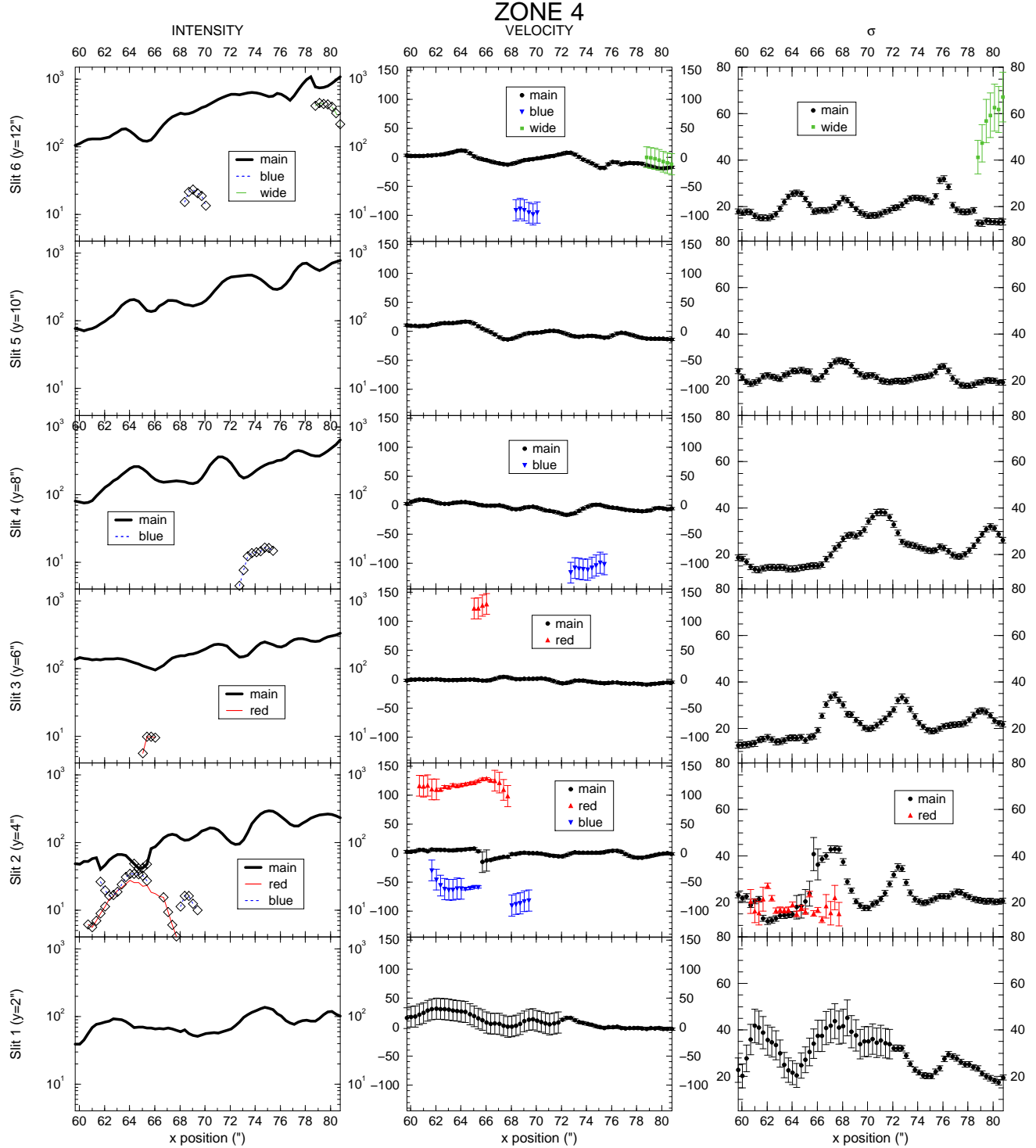


**Fig. 8.** Intensity, velocity and  $\sigma$  values fitted to the H $\alpha$  emission corresponding to the spectra of zone 4. Symbols, lines, slit separation, horizontal scale and units are as in Fig. 2. Note that in this case we have been able to assign a  $\sigma$  value to a secondary component (compare with, e.g., Fig. 2), the wide component on slit 6.

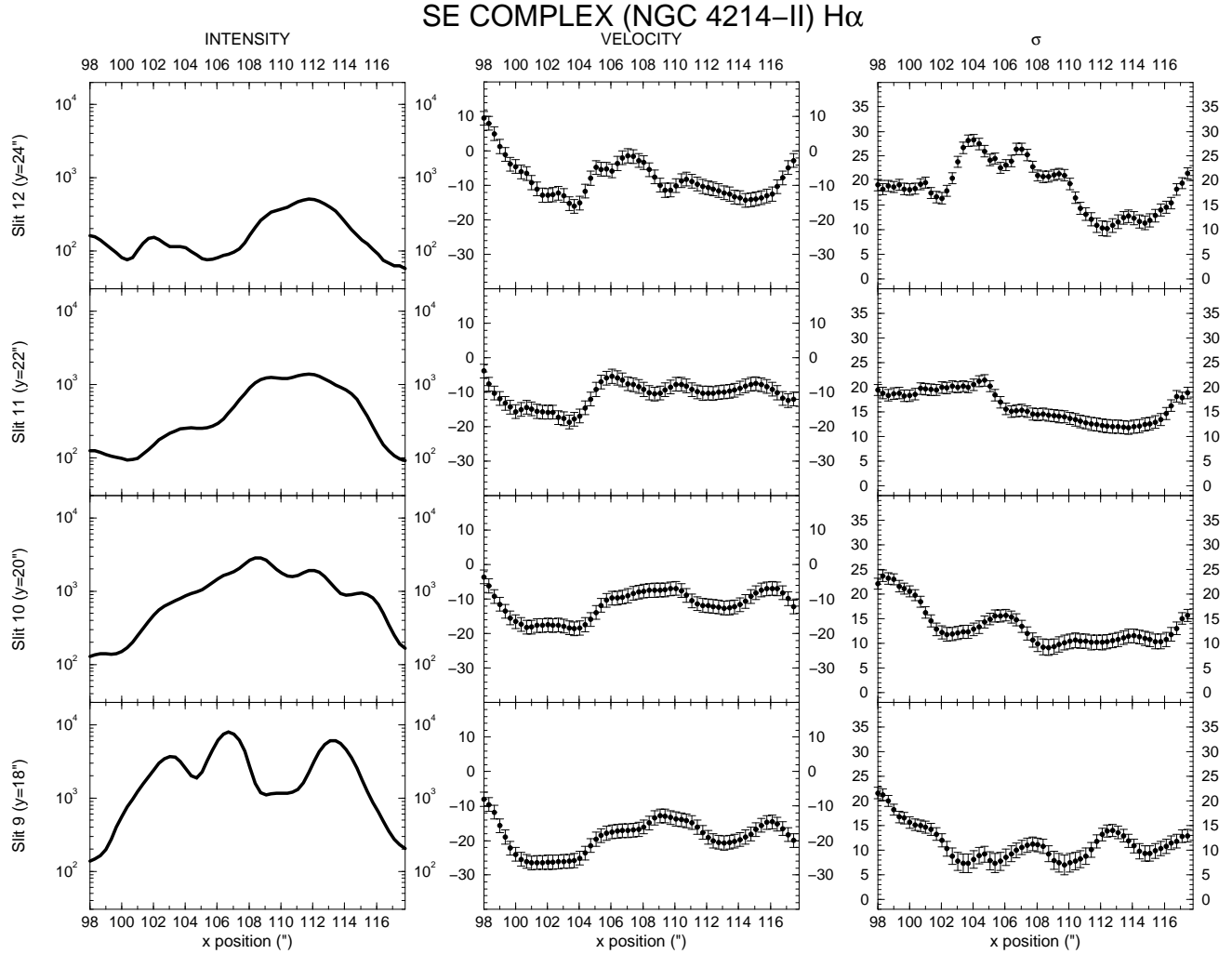


**Fig. 9.** Intensity, velocity and  $\sigma$  values fit to the H $\alpha$  emission corresponding to spectra from zone SE. Symbols, lines, slit separation, horizontal scale and units are as in Fig. 2. The positions of continuum knots E, D and K are nearly coincident with the three intensity maxima on slit 9.

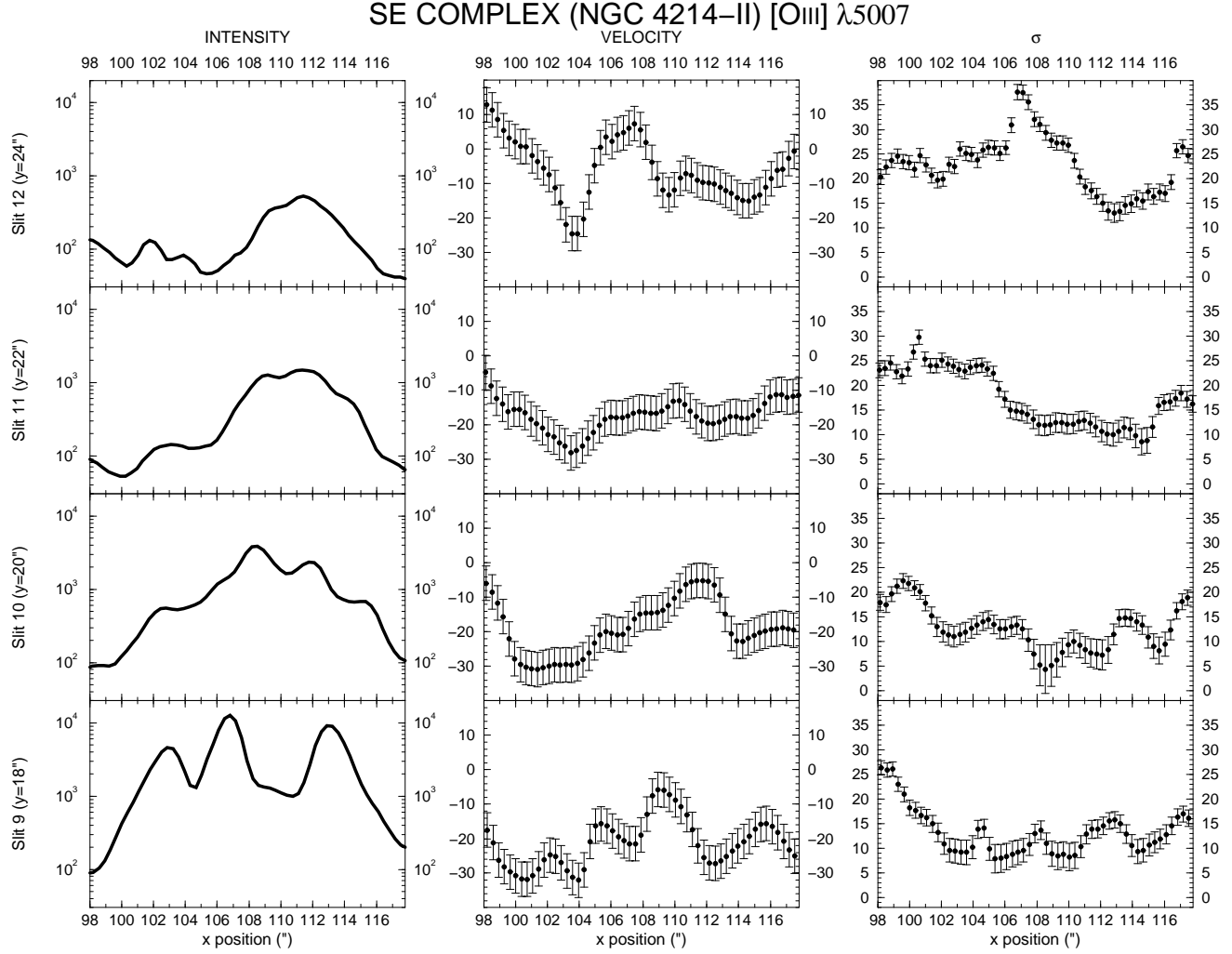


**Fig. 10.** Intensity, velocity and  $\sigma$  values fit to the [O III]  $\lambda 5007$  emission corresponding to spectra from zone SE. Symbols, lines, slit separation, horizontal scale and units are as in Fig. 2. The positions of continuum knots E, D and K are nearly coincident with the three intensity maxima on slit 9.

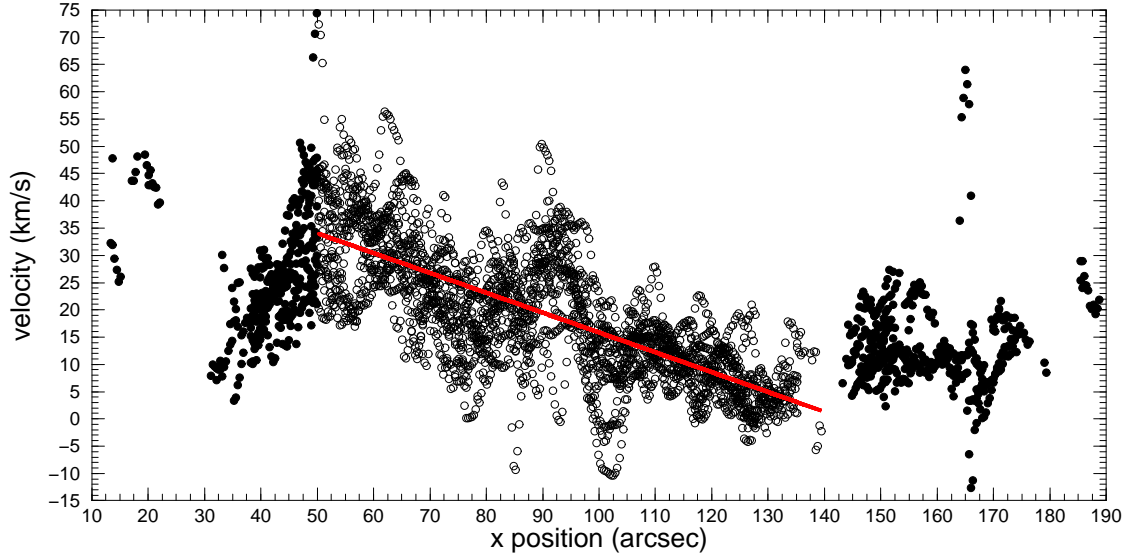


**Fig. 12.** Rotation curve in H $\alpha$  along the bar of NGC 4214 compressed along the direction perpendicular to the slit. The velocity corresponds only to the main (highest intensity) component in each pixel. Only those pixels with integrated intensity greater than  $20 \cdot 10^{-17}$  erg s $^{-1}$  cm $^{-2}$  arcsec $^{-2}$  are included. The straight line is a linear fit for the points with  $50'' \leq x \leq 140''$  (those represented as empty circles).